34th Symposium on Naval Hydrodynamics
Washington, D.C., June 26 - July 1, 2022

Experimental Investigation on the Wake of the Japan Bulk Carrier Model with Stereoscopic and Tomographic Particle Image Velocimetry

A. Sahab, P. Sumislawski and M. Abdel-Maksoud
(Institute for Fluid Dynamics and Ship Theory,
Hamburg University of Technology (TUHH), Germany)

ABSTRACT

To provide reliable turbulence data for validating computational fluid dynamics solvers, extensive experimental investigations are conducted on the wake of a double-body model of the underwater hull of the Japan Bulk Carrier without appendages in straight ahead and drift conditions in the low speed wind tunnel of TUHH. The investigation focused on capturing and tracking the After-Body (ABV) and Fore-body Side (FSV) vortices, using a Tomographic Particle Image Velocimetry (TPIV) system. The results of the investigation are compared with the results of an earlier investigation conducted in the same facility using a Stereoscopic Particle Image Velocimetry (SPIV) system in both straight ahead and drift condition. The results were compared additionally to the results of the investigation conducted by National Maritime Research Institute (NMRI) and Osaka University (OU) in a towing tank using a SPIV system for the straight ahead condition. In addition, this paper provides data for local flow fields and turbulence with high temporal and spatial resolution for future comparisons.

INTRODUCTION

Enhancing the ships manoeuvrability requires a deep understanding of the separated flow onset and its progression. As the wake of ships at high drift angles is strongly dominated by large separation areas and complex vortical structures, many experimental investigations were conducted in recent years on different types of ships in both straight ahead and static drift conditions, e.g. the experiments of Abdel-Maksoud, *et al.* (2016) on KVLCC2 model, Broglia, *et al.* (2012) on DELFT 372 catamaran model and Egeberg, *et al.* (2014) on a surface combatant ship hull. Although all investigations were able to successfully evaluate the local flow data, there remains still a lack of reliable validation data for turbulence. Despite the great progress in the computational fluid dynamics (CFD) solvers in the last 30 years, an accurate evaluation of the vortical structures is still a challenge due to this lack of reliable validation data.

Continuous developments of measurement systems have led to more efficiency and an increased quality of the measured data. An important example is the Tomographic Particle Image Velocimetry (TPIV), which is based on measuring a coherent 3D flow volume at possibly high sampling rates. A TPIV combined with high spatial discretization is a powerful measuring system to investigate turbulent and highly unsteady flows. An important example for the successful utilization of TPIV system in investigating complex vortex structures is demonstrated by the work of Bhushan, *et al.* (2021) on the flow patterns for surface combatant 5415 at straight-ahead and static-drift conditions.

Hamburg University of Technology (TUHH) operates a low-speed wind tunnel. In 2020, a TPIV system has been put into operation in order to conduct extensive studies of turbulent flow in the wake of the Japan Bulk Carrier (JBC), which is selected as one of the test cases for the workshop on CFD in ship hydrodynamics in Tokyo 2015, Hino (2017). National Maritime Research Institute (NMRI) along with other partners were involved in designing the JBC and its appendage. NMRI (Hino, *et al.* (2016)) and Osaka University (OU) (Jufuku, *et al.* (2015)) conducted a series of experiments in a towing tank to identify the stern flow fields, amongst others, using a stereoscopic Particle Image Velocimetry (SPIV). However, these investigations were focused on the straight-ahead condition with and without a propeller and energy-saving device (ESD), while the static-drift condition was not investigated.

The stern flow fields were previously investigated in the TUHH wind tunnel using SPIV. The results were presented in Shevchuk, *et al.* (2020). The earlier investigation conducted at TUHH was able to provide adequate data for the local flow fields. However, the quality of the turbulence data was not sufficient to be

considered as a reference for CFD code validation.

The main objective of this study is to conduct a detailed flow structure investigation on the wake of the JBC hull without appendages in a straight ahead as well as drift conditions using the new state-of-the-art TPIV system. Furthermore, an extensive set of measurement data with high temporal and spatial resolution is being made accessible for CFD code validation. Beyond that, the evolution of the vortical structure is investigated so that vorticity and turbulent kinetic energy are estimated in the vortex core.

APPROACH

The investigation is conducted on a double body model of the underwater hull of the JBC in which the hull is mirrored around the selected waterline in a low-speed wind tunnel at TUHH. The wind tunnel has a test section of rectangular cross-section ($2m \times 3m$) and a length of $5.5m$. The low-speed wind tunnel at TUHH can be operated in an either closed (Göttingen) or open (Eiffel) loop mode, thus it is an outstanding facility which can be used to investigate the hydrodynamics of sub-surface objects as well as underwater hulls. The open-return configuration is shown in Figure 1. The technical data for the test section of the wind tunnel is shown in Table 1. For this investigation, the closed loop configuration (Göttingen) was used for the wind tunnel to maintain a constant temperature and characteristics for the airflow.

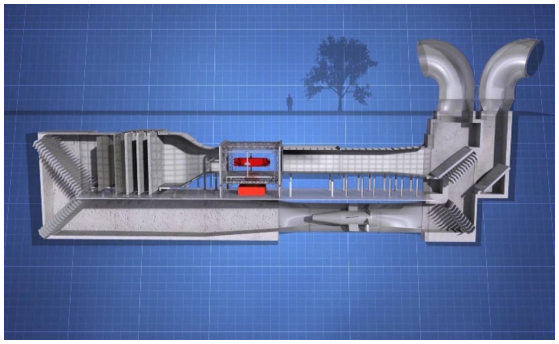

Figure 1: The low speed wind tunnel of TUHH in Eiffel (open-return) configuration

The motion simulator has a similar design concept to the one proposed by Merlet (2008). The main parameters of the ship in comparison to the model are shown in Table 2, while the main dimensions of the model are illustrated in Figure 2. Two identical models were used for the experimental investigations. The former one was built several years ago to perform SPIV measurements in order to investigate the flow around the model, but the configuration did not allow for conducting force measurements. Therefore, a new model was built in which a 6-component scale was integrated. The second model was used for the current investigation using the TPIV system.

Table 1: Technical data for test section of the wind tunnel

Dimensions	L 5.5m, W 3m, H 2m
Maximum Wind Velocity	35 m/s
Nozzle's Contraction Ratio	4.125
Fan Unit Power	400 KW
Degree of Turbulence	$< 0.3\%$
Traversing Mechanism Accuracy	< 0.1 mm

Table 2: Main parameters of the ship and the model

	Symbol	Unit	Ship	Model
Length overall	L_{oa}	[m]	291	3.651
Length between perpendiculars	L_{pp}	[m]	280	3.513
Breadth (waterline)	B	[m]	45.2	0.565
Draft (original)	T	[m]	16.6	0.208
Block coefficient	C_B	[-]	0.848	0.848
Scale ratio	λ	[-]	1	79.7

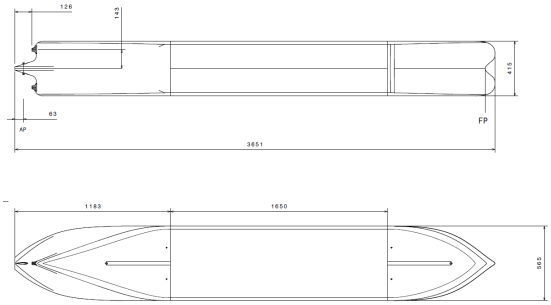

Figure 2: Main dimensions of the JBC model

As shown in Figure 3, the model is mounted on the motion simulator of the wind tunnel. The flow velocity fields in the vicinity of the coherent vortices were measured by Tomographic Particle Image Velocimetry system (TPIV) to conduct a comparison with the earlier published results in Shevchuk, *et al.* (2020) which were measured using a SPIV. The same coordinate system is used according to which the origin is located at the

intersection between the After-Perpendicular (AP) and the water plane. The x-axis is directed upstream, the z-axis is vertically upwards and thus the y-axis is directed towards port side according to the right-hand rule. This coordinate system is visualized in Figure 4.

Figure 3: JBC double hull mounted on motion simulator in the low speed wind tunnel of TUHH

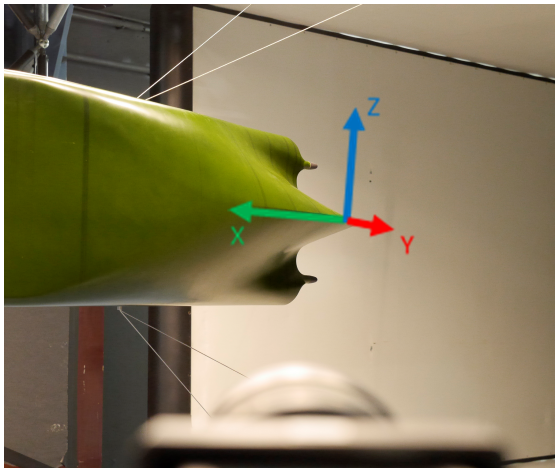

Figure 4: Coordinate system for measurement systems

This investigation focuses on two main vortex structures; the After-Body Vortex (ABV) and the Fore-body Side Vortex (FSV), see Figure 5 and Figure 6. The separation for ABV occurs at the ship stern. Due to complex flow structure in the stern region of the JBC, the influence of this vortex on the flow in this region is of high interest. Understanding the flow structure in this region is essential for further investigations which include propeller performance and energy saving devices (ESD) in order to improve the propulsive efficiency. The separation of FSV takes place much further upstream close to the forward shoulder and it progresses along the lee side of the hull. Since the FSV propagates in the vicinity of the model and a high laser reflection on the hull can be observed, it is possible to track and capture this vortex only in the furthest downstream positions.

The measurement stations for the ABV in the straight ahead condition introduced in Hino (2017) were considered in the study. The ABV dominates the wake of the JBC hull in straight-ahead condition. For the static-drift condition, additional measurement stations are introduced to track the FSV. The positions of measurement planes for both conditions are depicted qualitatively in Figure 5 and Figure 6 for straight-ahead and drift conditions respectively. The exact positioning of the measurement stations for both ABV and FSV in the current investigation as well as the measurement stations for the earlier SPIV measurements are given in Table 3. The measurement station S7 is positioned at the AP. The positions of both vortical structures are approximated by CFD calculations, which is needed for the correct positioning of the TPIV measurements. The detailed description of the CFD methods used - such as Reynolds-Averaged Navier-Stokes (RANS), Delayed Detached-Eddy Simulation (DDES) and Improved Delayed Detached-Eddy Simulation (IDDES) - as well as their corresponding results used for this prediction is elaborated in detail in Sumislawski (2022).

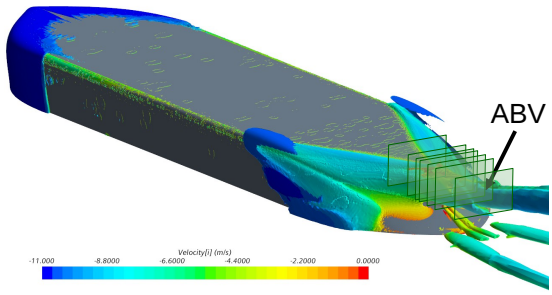

Figure 5: Qualitative positioning of measurement planes at ABV for straight ahead condition

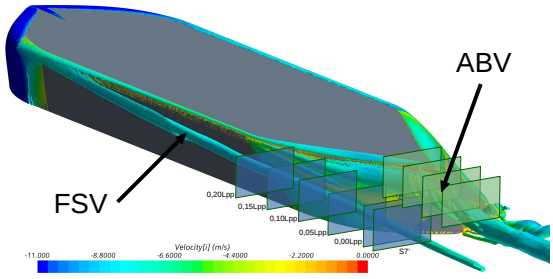

Figure 6: Qualitative positioning of measurement planes at FSV and ABV for drift condition

Table 3: Measurement stations

Plane	$x_s[mm]$	$x_s/L_{pp}[-]$	SPIV	ABV	FSV
S7'	-062.9	-0.0179		✓	✓
S7 (AP)	000.0	0.0000	✓	✓	✓
S6	027.1	0.0077	✓	✓	
S5	047.8	0.0136	✓		
S4	055.2	0.0157	✓	✓	
S4'	066.4	0.0189		✓	
S3	074.3	0.0211	✓		
S3'	098.4	0.0280		✓	
S2	131.7	0.0375	✓		
S1	175.7	0.0500	✓	✓	✓
X0p10	351.3	0.1000			✓
X0p15	527.0	0.1500			✓
X0p20	702.6	0.2000			✓

Test Conditions

An inflow air velocity of $U_\infty = 10m/s$ is used for the straight-ahead and drift tests alike. Due to the negligible temperature variation, the Reynolds number can be considered constant at 2.42×10^6. The model is restrained from all free motions because of the fixation on the motion simulator. A drift angle of 8° is applied for drift measurements and was obtained by adjusting the orientation of the model with the motion simulator. The blockage ratios of the wind tunnel were 0.04 and 0.06 for the straight-ahead and drift measurements respectively.

Zigzag stripes were used on the model bow for turbulence stimulation and their positioning was in accordance with the recommendations of the 26th ITTC (2011): Z_1 at $1.4\%L_{pp}$ upstream of the Forward Perpendicular (FP) ($1/3$ of the bulb length of the bulbous bow from its fore end), Z_2 at $5\%L_{pp}$ aft of the FP and Z_3 at shortly before the expected position of the positive pressure gradient approximately $8.8\%L_{pp}$ aft of FP as shown in Figure 3. The influence of the turbulence stimulation was not experimentally investigated within the scope of this work.

Stereoscopic Particle Image Velocimetry System

The SPIV consisted of a pulsed laser, a light sheet optic and two cameras. The light sheet was generated by a $200mJ$ two-headed Nd:YAG-laser (Quantel Big Sky). The two PowerView 4MP (2048×2048 pixels, $12bit$, monochrome) cameras equipped with AF-S Nikkor $300mm/F4D$ IF-ED lenses captured the scattered light from the seeding particles. The cameras baseline is positioned around $1.7m$ from the centre of the test section. Since the optical axis of the lenses are inclined 61° and 44° to the normal of the laser plane, Scheimpflug adapters were used to adjust the angle between the cameras and their lenses meeting Scheimpflug condition. A short time separation of $25\mu s$ is used to minimise the loss of particles between the two frames captured by each camera. This value was defined to ensure that the particles do not travel more than 25% of the light sheet thickness. The measurements were conducted with $7.25Hz$ sampling frequency.

A Laskin type droplet generator uses Di-Ethyl-Hexyl-Sebacat (DEHS) to generate the seeding particles. To ensure homogenous global distribution of particles in the test section, the particles are injected downstream of the test section and they follow the air flow throughout a complete loop in the wind tunnel before reaching the test section. Therefore, any influence due to turbulence of the generated fog is negligible.

Different techniques such as Fast Fourier Transformation, cross correlation techniques and ensemble averaging of the calculated correlation maps were used to analyse the captured images. The location of the correlation peak with sub-pixel accuracy was determined by the means of Gaussian curve fitting. The results were calculated with a 50% overlap of neighbouring vectors for the two-component vector maps of each camera. Reconstruction of three component velocities was based upon the vector maps of both cameras as well as calibration data. The calibration process was conducted using a black target with a predefined rectangular grid of dots spread on two planes. The whole SPIV was installed on one crossbar that can be moved by a traversing mechanism in both vertical and horizontal direction. Such configuration allows the usage of the same calibration set for the different measurement stations while maintaining the same camera and laser configuration.

In order to increase the dimensions of the total measured plane, high resolution 1000 focused images in the form of a 5×3 matrix (i.e.: 5 rows and 3 columns of 1000 images) were captured at each measuring station. A sufficient overlap between neighbouring images is maintained across the matrix. An overlap algorithm is used to produce the final full result by constructing a grid with a grid offset of $1.886mm$ that is equivalent to the grid offset of the individual positions to prevent any aliasing effects.

Tomographic Particle Image Velocimetry System

The TPIV is composed of a total of four cameras and a laser with laser optics in addition to a laser arm which is used to facilitate the positioning of laser optics. The

light volume for TPIV measurements is generated by a 40 mJ dual cavity Nd:YLF-laser (Photonics Industries). The four Phantom Veo 440L $4MP$ (2560×1600 pixels, $12bit$) cameras equipped with Nikkor $180mm/F2.8$ lenses are capable of capturing the frames at a maximum sampling frequency of $1.1KHz$ for a single frame configuration. Since double frames are needed for TPIV analysis, 3000 double frames were captured with a sampling frequency of $500Hz$ and time separation of $60\mu s$. Similar to SPIV configuration, Scheimpflug adapters are used for all cameras. The camera, laser, laser arm and laser optics are shown in Figure 7. The same seeding hardware and techniques used in the SPIV measurements were utilized again.

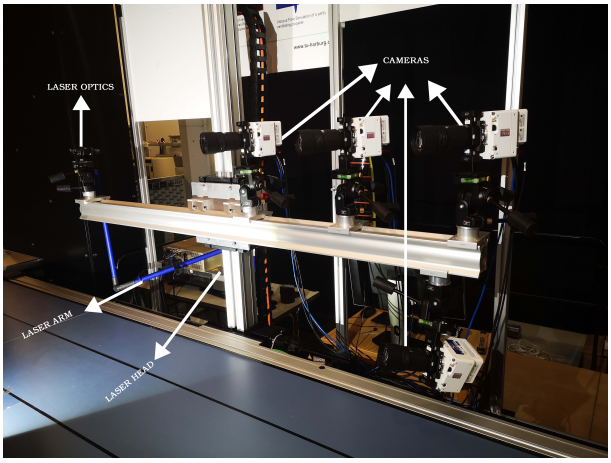

Figure 7: TPIV system mounted on a traversing mechanism in the low speed wind tunnel of TUHH

The calibration process is conducted using the standard 309-15 calibration target provided by LaVision GmbH. The target is a double-plane, double-sided $309mm \times 309mm$ black target with a thickness of $14.8mm$ and plane-to-plane distance of $3mm$. The calibration target has a grid of 21×21 white circles of a size $3mm$ and grid spacing of $15mm$. In order to calibrate the desired volume, the measurement system mounted on a beam was traversed in a streamwise direction at steps of $1.5mm$ and in a total of 9 calibration planes. Since the positions of the cameras are kept fixed relative to each other, the same calibration can be used for all measurement positions and a new calibration at each measurement position can be avoided. This approach has the advantage of ensuring no deviations between different measurement stations due to variations in the system calibration.

Data Reduction

The vector fields were obtained using DaVis 10.2 software provided by LaVision GmbH. Since the measurements are conducted on a static ship model, the laser reflections on the model hull can be safely assumed to be constant over time and therefore the images were preprocessed by using a filter to subtract the minimum over time with a size of 9 consecutive images. A geometrical mask was used to exclude the ship model along with any reflections on its hull. In order to remove the images background, a filter is used to subtract the sliding minimum of 3 neighbouring pixels. To better identify the particle positions, a sequence of different filters was used to normalise each image with local average over 1000 pixels then all frames were normalised to the first frame, sliding Gaussian smoothing followed by a sharpening filter and finally multiplying the intensity of each pixel with a factor of 10 to increase the difference between the particles and the background.

A volume of approximately $6mm \times 310mm \times 120mm$ was reconstructed from the double frames captured by the four cameras. The correlation was applied using multi-pass approach in 4 steps as shown in Table 4. A circular grid was used for the correlation with an overlap of 75% for all steps. In post-processing, vectors with correlation coefficient below 0.4 were removed.

Table 4: Correlation Parameters for tomographic reconstruction

Step	Passes	Size [vox]	Search radius	Binning [vox]
1	1	96	8	$8 \times 8 \times 8$
2	2	80	4	$4 \times 4 \times 4$
3	1	64	2	$2 \times 2 \times 2$
4	4	48	1	no

In order to obtain a field of view comparable to the earlier results by SPIV, three overlapping measurement windows are captured at each station. The windows form an array in the vertical direction and the overlap between them is selected to be sufficient to avoid any discontinuity in the results. The final overlapped results have a volume of approximately $4.4mm \times 307mm \times 220mm$ with a spatial resoultion of $1.1mm$. The dimensionless values were obtained by using the following normalizations:

- Positions: using L_{pp}
- Velocity component (U_x): using U_∞
- Velocity components (U_y & U_z): using $|U_\infty|$
- Vorticity vectors: using $|U_\infty|/L_{pp}$
- Mean and Turbulent Kinetic Energy: using U_∞^2
- Swirl: using $(U_\infty/L_{pp})^2$

Uncertainty Analysis (UA)

The UA follows the Performance Test Code (PTC) proposed by the American Society of Mechanical

Engineers (ASME) 19.1-1998 by ASME Text Code (1998) and its revision 19.1-2005 by ASME Text Code (2006). The UA is divided into two main analyses in which the systematic standard error (b_x) and the random standard error (S_x) are evaluated individually for any variable x. The combined standard uncertainty is hence deduced as the root sum of the systematic and random standard error squares and finally the expanded uncertainity is defined based on the selected confidence level.

The systematic standard error is dependant on the elemental error sources. The elements to be considered are the positioning of measurement system and model. The uncertainties of the positioning for the traverse system, on which the measurement system is mounted, is $b_{ms} = \frac{B_{ms}}{2} = 5 \times 10^{-5} m$, of the position and orientation of the motion simulator, on which the model is mounted, is $b_{mp} = \frac{B_{mp}}{2} = 5 \times 10^{-5} m$ and $b_{mo} = \frac{B_{mo}}{2} = 8.5 \times 10^{-4} rad$, where $B_{ms} = 0.0001m$, $B_{mp} = 0.0001m$ and $B_{mo} = 0.0017rad$. The systematic standard uncertainties are $b_{\overline{u},\overline{v},\overline{w}} = 0.000853$ for all velocity components u, v and w.

The random standard error is evaluated using the $N = 3000$ recordings measured at measurement station $S7$ for the middle measurement window. The random standard uncertainties are $S_{\overline{u}} = 0.0169$, $S_{\overline{v}} = 0.0162$ and $S_{\overline{w}} = 0.0113$. The total uncertainty for the velocity components are $u_u = \sqrt{b_{\overline{u}}^2 + S_{\overline{u}}^2} = 0.0169$, $u_v = \sqrt{b_{\overline{v}}^2 + S_{\overline{v}}^2} = 0.0162$ and $u_w = \sqrt{b_{\overline{w}}^2 + S_{\overline{w}}^2} = 0.0113$. The expanded uncertainties are $U_{\overline{u}} = 0.0338$, $U_{\overline{v}} = 0.0324$ and $U_{\overline{w}} = 0.0226$.

SPIV VS TPIV

The measurement configuration of cameras and laser optics in both cases of SPIV and TPIV are considerably similar. However, multiple other factors impact the quality of the results. First of all, the camera sensors are rectangular in the case of TPIV with lenses of $180mm$ focal length and thus have a wider field of view in comparison to SPIV with its square camera sensors and lenses of $300mm$ focal length. This wider view has the advantage that the required width is captured within one recording series which would eliminate the need for recording multiple lateral neighbouring measurement windows and thus avoid errors due to the overlapping between these windows. The increase in width of the measurement windows was accompanied by a decrease in height for field of view, however only 3 measurement windows were sufficient to cover the required investigation volume. The decrease in spatial resolution due to usage of lenses with smaller focal length was compensated by using interrogation areas with higher overlap.

Minor deviations between the current TPIV and the previous SPIV results are expected due to some additional factors; model surface roughness, sampling frequency and measurement duration. Since a new ship model is constructed for the newly-planned investigations with the TPIV system, the surface roughness cannot be exactly reproduced by the model manufacturer. As the TPIV has a much higher sampling frequency, it is expected that the TPIV would be able to capture the high frequency flow characteristics that the SPIV would usually miss. However, this higher frequency of TPIV comes at the cost of the measurement duration due to the storage capacity requirements, thus the TPIV might miss some very low frequency characteristics of the flow.

In order to ensure that a statistical convergence is reached, 3000 recordings were taken for each measurement window instead of much fewer recordings in the case of SPIV. The statistical convergence of the total velocity at the points $P_1 = (0, 0.0142, -0.0353)$ in the vicinity of the ABV vortex, point $P_2 = (0, 0.0441, -0.0563)$ in the free-stream and point $P_3 = (0, 0.0157, -0.0573)$ in the vicinity of the shear layer in the S7 measurement plane for the drift condition is shown in Figure 8, while the same is shown in Figure 9 for the standard deviation of the total velocities. A convergence threshold of 0.5% from the final value is reached at P_2 with only 175 recordings, while 1000 recordings were required to reach such threshold for both P_1 and P_3 due to the turbulence behaviour in their vicinity. The full range of the 3000 recordings was required to reach a statistical convergence for the standard deviation of the total velocity.

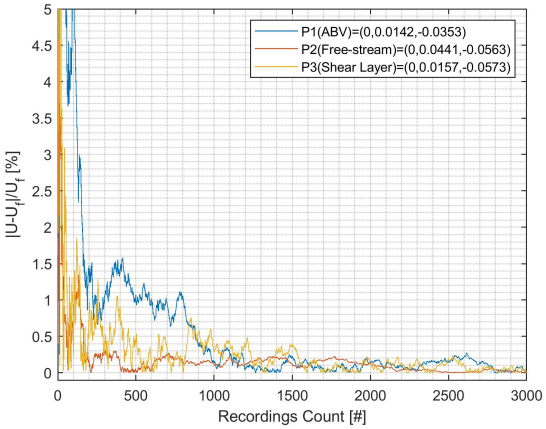

Figure 8: Statistical convergence of the total velocity

The approach introduced by Levy, *et al.* (1990) using vortex helicity to track the vortex core is adopted within this investigation. However, since

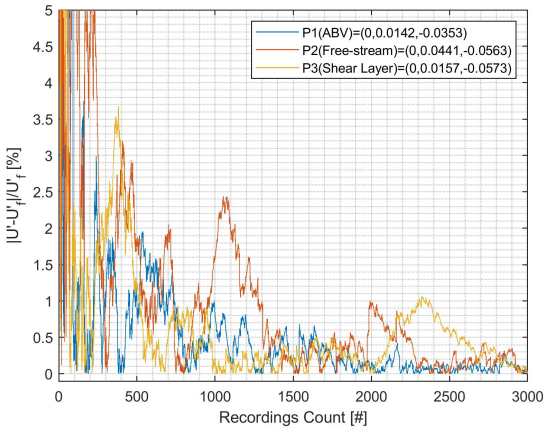

Figure 9: Statistical convergence of standard deviation of total velocity

the vortex helicity is not available for the earlier SPIV measurements, the maximum vorticity component around x-axis (ω_x) will be used in this paper instead of a maximum helicity so that the results from both measuring systems can be compared. The normalised helicity of a vortex is computed using the formula 1, where V is the velocity field and ω is the vorticity field.

$$H_n = \frac{V.\omega}{|V||\omega|} \tag{1}$$

Figure 10a shows an example for the helicity at measurement station S7 for the drift condition. The region with the maximum range of helicity in the ABV is bounded by the red line. Figure 10b shows the same figure plotted with a different color scale to focus on the regions where the maxima of helicity exists and thus defining the vortex core.

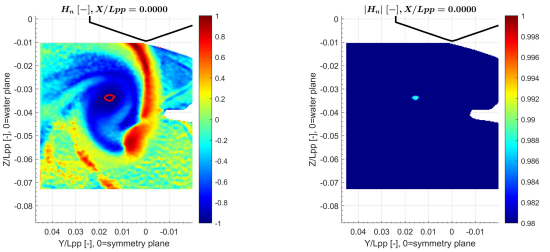

(a) Helicity full color scale **(b)** Helicity Vortex Core

Figure 10: Helicity at S7 in drift condition

Straight Ahead Case Results

Since the earlier investigations at TUHH using SPIV and the ones conducted at OU as well as NMRI were conducted at measurement stations S4 as well as S7 only and focused mainly on the ABV, the comparisons between TPIV results and others will only be conducted at the before-mentioned stations. The results of the CFD prediction of the vorticity magnitude for the ship in straight-ahead condition is shown in Figure 11. It is expected that the vorticity is initially concentrated at the shear layer and consequently at two regions - the shear layer and the ABV core. It is also expected that the vorticity magnitude at the ABV core outlasts the shear layer.

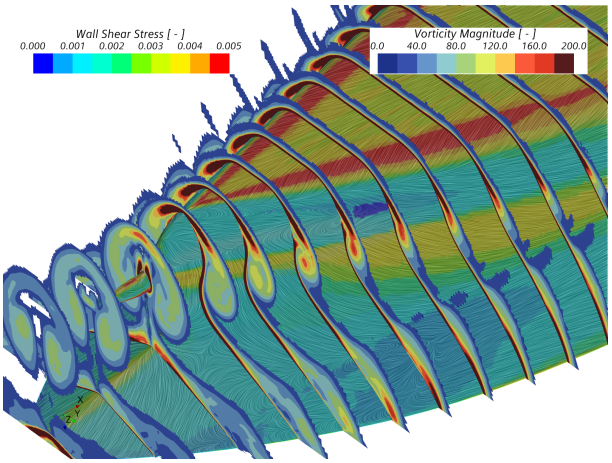

Figure 11: CFD approximation using IDDES for vorticity magnitude in straight ahead condition

The velocity field was measured at the different stations, from which the vorticity, the Turbulence Kinetic Energy (TKE), Reynold stress tensors and Helicity were calculated. Figures 12 and 13 represent the velocity component in the streamwise direction for ABV. Although the low velocity region is clearly symmetric around the symmetry plane and complies with the previous measurements, the minimal velocity regions by the TPIV system are around one step higher in measured speed. This can be clearly seen in Figure 13b, where the minimal normalised speed contour in the shear layer is 0.25 instead of the earlier 0.2 and in the vicinity of ABV is 0.45 instead of the earlier 0.4.

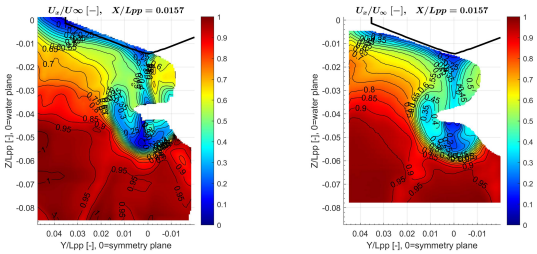

(a) SPIV **(b)** TPIV

Figure 12: U_x at S4 in straight ahead condition

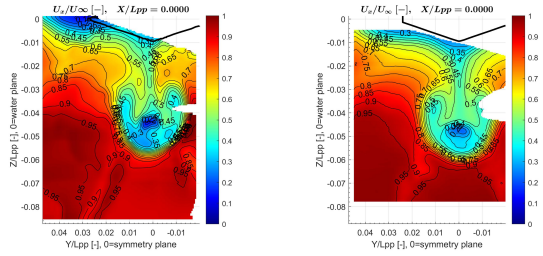

(a) SPIV **(b)** TPIV

Figure 13: U_x at S7 in straight ahead condition

The transversal velocity component U_y is illustrated in Figures 14 and 15 for measurement stations S4 and S7 respectively. The TPIV results show higher consistency regarding the large negative contour region (iso-line -0.20 at S4 and -0.15 at S7), while a much weaker velocity gradient at the shear layer area was detected. An anti-symmetric velocity profile is clear.

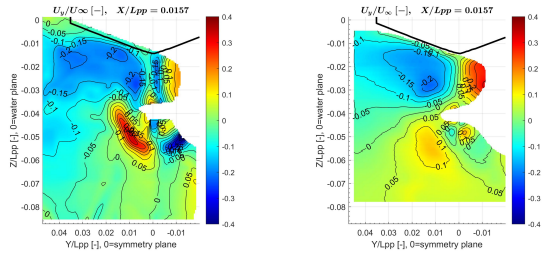

(a) SPIV **(b)** TPIV

Figure 14: U_y at S4 in straight ahead condition

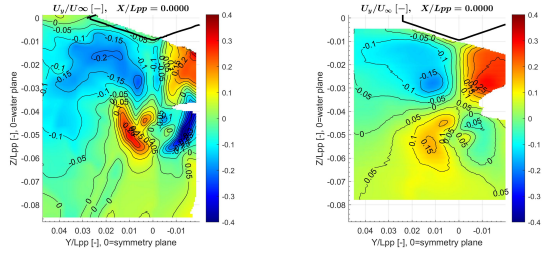

(a) SPIV **(b)** TPIV

Figure 15: U_y at S7 in straight ahead condition

The vertical velocity component U_z is illustrated in Figures 16 and 17 for measurement stations S4 and S7 respectively. The TPIV results are almost identical to the previous SPIV measurements. A minor deviation is noted in the smaller area enclosed by the 0.25 iso-line on the port side at measurement station S4 and the its complete disappearance at S7. Otherwise, the vertical velocity component has a symmetrical velocity profile.

Although the vorticity component around the

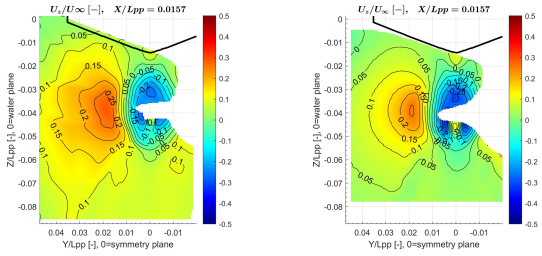

(a) SPIV **(b)** TPIV

Figure 16: U_z at S4 in straight ahead condition

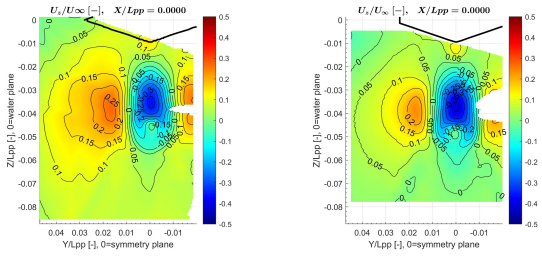

(a) SPIV **(b)** TPIV

Figure 17: U_z at S7 in straight ahead condition

x-axis for both measurement stations S4 and S7 are qualitatively comparable to the earlier results of the SPIV where a major vortex structure surrounds a smaller one as illustrated in Figures 18 and 19, the minor vortical structures appearing at around $Z/L_{pp} = -0.055$ and on both sides of the symmetry plane are not further realised in the TPIV results. As illustrated in Figure 20, these minor vortical structures are also not realised by the other research institutions NMRI and OU, which would give higher credibility to the new TPIV measurements.

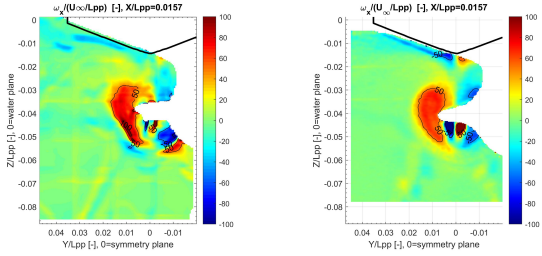

(a) SPIV **(b)** TPIV

Figure 18: ω_x at S4 in straight ahead condition

One of the main advantages of the TPIV over the earlier SPIV measurements is the ability to capture the out-of-plane vorticity components (i.e.: ω_y and ω_z) as demonstrated by Figures 21a and 21b for the measurement station S7 in straight ahead condition respectively. The vorticity component ω_y is highly concentrated in the shear layer curving the layer into the

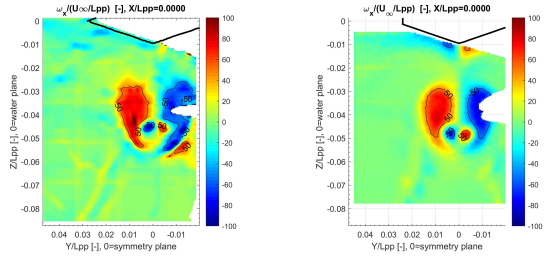

(a) SPIV **(b)** TPIV

Figure 19: ω_x at S7 in straight ahead condition

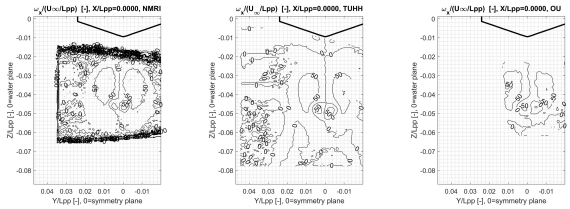

(a) NMRI SPIV **(b)** TUHH TPIV **(c)** OU SPIV

Figure 20: ω_x at S7 in straight ahead condition for different research institutions

upwards direction along the streamwise direction. An anti-symmetric ω_z vorticity component, where the highest intensity lies outside of the ABV region, is detected.

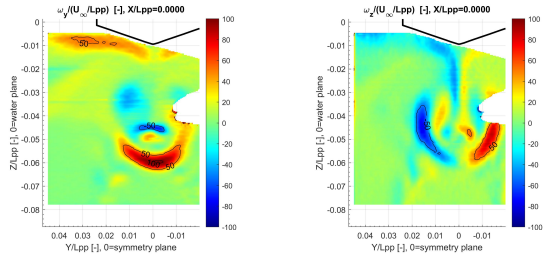

(a) ω_y **(b)** ω_z

Figure 21: ω_y and ω_z at S7 in straight ahead condition

Since all vorticity components could be realised by the TPIV, the evaluation of the total vorticity (ω) can be computed, as shown in Figure 22.

The fewer measurement windows and their overlapping in the case of TPIV provided the advantage that the measured data are more temporal consistent. The lower overlapped windows count boosts the possibility to minimize errors due to the inaccuracy of the overlap post-processing process. These errors might be noticed visually at $Z/L_{pp} = -0.020$ and $Z/L_{pp} = -0.032$ in Figure 23b for example. At these two regions, minor distortions can be realized, which have no physical interpretation. However, these distortions have no major influence of the overall quality of the results.

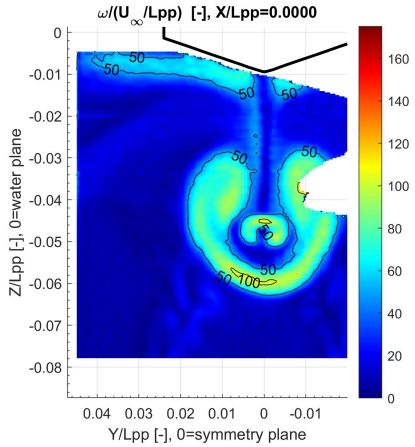

Figure 22: ω at S7 in straight ahead condition

Figures 23 and 24 illustrate the TKE at the measurements stations S4 and S7 respectively. The high intensity of TKE is focused mainly in the shear layer and at the wake of the propeller axis. It extends upwards as well to the vicinity of the ABV, however with a less energy content.

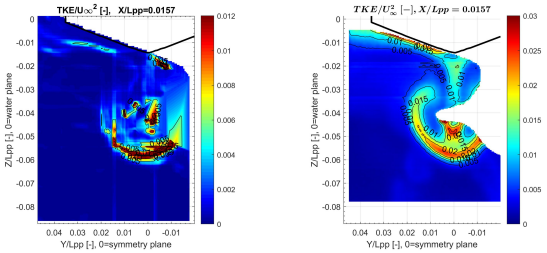

(a) SPIV **(b)** TPIV

Figure 23: TKE at S4 in straight ahead condition

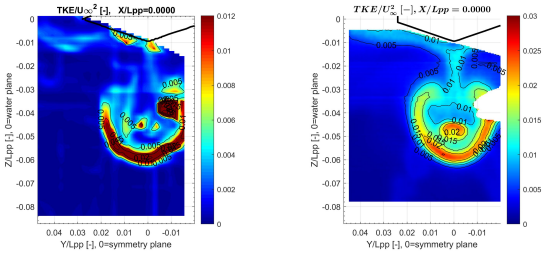

(a) SPIV **(b)** TPIV

Figure 24: TKE at S7 in straight ahead condition

The TPIV results show higher capabilities of capturing the energy profile, despite having a two-fold higher TKE level. A higher TKE level compared to earlier SPIV results is also measured by OU as illustrated in Figure 25. However, the turbulent energy level captured

by OU deviates from the recent results with TPIV; around 0.010 instead of 0.015 at ABV's region and around 0.025 instead of 0.020 at the shear layer. Unfortunately, there is no data available for TKE from NMRI for comparison.

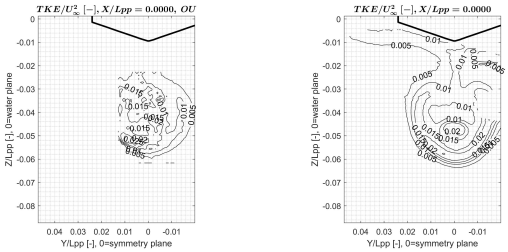

(a) OU **(b)** TUHH

Figure 25: TKE at S7 in straight ahead condition for different research institutions

A clear advantage of the TPIV is the ability to evaluate the Reynolds stress tensors. An example of the diagonal tensors (i.e.:R_{xx}, R_{yy} and R_{zz}) for measurement station S7 in straight-ahead condition are illustrated in Figure 26, while the non diagonal tensors (i.e.:R_{xy}, R_{xz} and R_{yz}) are illustrated in Figure 27. The tensors R_{xx}, R_{yy}, R_{zz} and R_{xz} show a decently symmetrical profiles. The R_{xy} and R_{yz} tensors show an anti-symmetrical profiles. The highest energy content of R_{xx} can be noticed in the shear region.

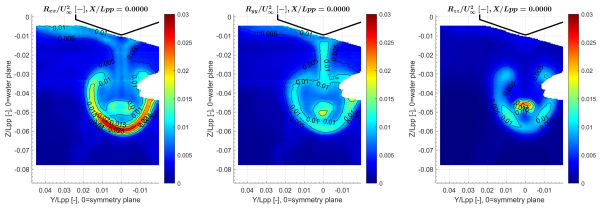

(a) R_{xx} **(b)** R_{yy} **(c)** R_{zz}

Figure 26: Reynolds diagonal tensors at S7 in straight ahead condition

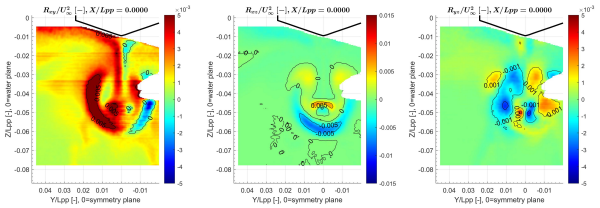

(a) R_{xy} **(b)** R_{xz} **(c)** R_{yz}

Figure 27: Reynolds non-diagonal tensors at S7 in straight ahead condition

The swirl ($\lambda 2$) is calculated following the method proposed by Jeong and Hussain (1995) and shown for S7 measurement station in Figure 28. The ABV on both sides of the symmetry plane can be clearly seen where a major vortex structure surrounds a smaller one as depicted earlier in Figure 19.

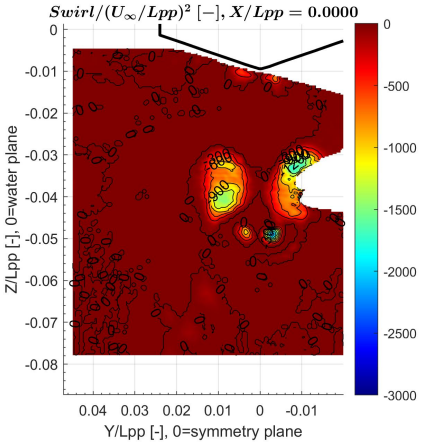

Figure 28: Swirl at S7 in straight ahead condition

A quantitative comparison between the SPIV, TPIV, NMRI and OU results at the measurement station S7 along the line $\frac{Z}{L_{pp}} = -0.0407$ representing the propeller axis horizontal plane is conducted. The results for the velocity component in the streamwise direction, the vertical velocity component, the vorticity around the x-axis as well as TKE are shown in Figure 29. Similar trends in the results of both SPIV and TPIV measurements systems are detected. The TPIV results show a higher smoothing tendency for the streamwise velocity component and the vorticity around x-axis. This is reasonable effect due to the higher recordings count in the case of the TPIV measurements and since vortex wandering effects are not eliminated in both results. The TKE profile in the TPIV results has a similar shape to the SPIV results, despite the higher detected level of energy content. The many overlapping windows in the SPIV case could be the main reason for such lower energy content. It can be clearly noticed that the data provided by the TPIV measurement system correlates better than the output of SPIV to the results provided by both NMRI and OU, in particular for the U_x near the symmetry plane, for ω_x and for TKE.

Drift Case Results

For the drift case, the results of the CFD prediction of the vorticity magnitude demonstrate that a considerable interaction occurs between ABV and FSV as shown in Figure 30. The same behaviour for the shear layer in straight-ahead condition can be still realised in the drift condition as the vorticity concentration diminishes quickly after separation and the vorticity in ABV core

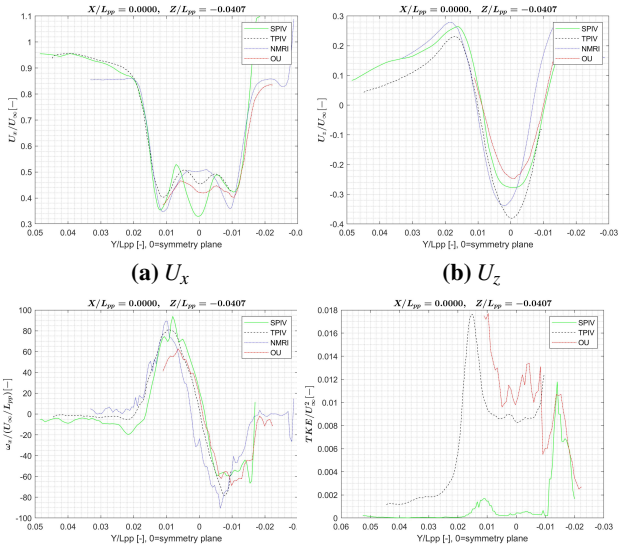

(a) U_x **(b)** U_z

(c) ω_x **(d)** TKE

Figure 29: Comparison at S7 along a line in the straight ahead condition

outlast the vorticity in the shear layer. Since the separation of FSV takes place in a much further upstream position, the vorticity magnitude in FSV core is much weaker compared to the ABV core when measured at the same measurement station.

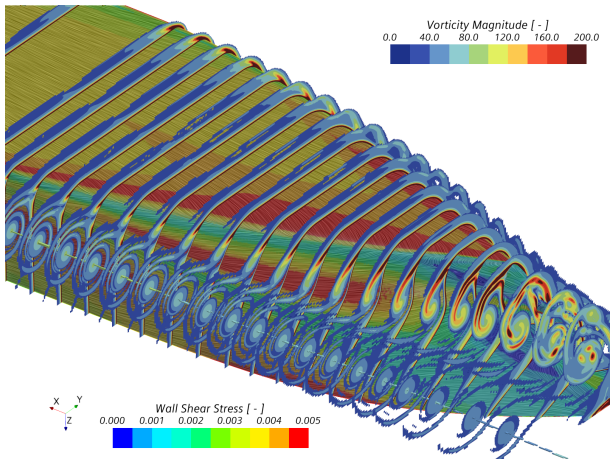

Figure 30: CFD approximation using DDES for vorticity magnitude in drift condition

The overall features for the axial velocity component, such as the low-velocity region forming a hook shape towards the leeward, are still realised. The axial velocity component shows in general very slight deviation of the velocity contours for the TPIV results in comparison to the previous SPIV results, as shown in Figures 31, 32 and 33 for measurement stations S1, S4 and S7 respectively. For example, the velocity iso-line of 0.6 between the ABV and the low velocity region is no longer discernible any more in Figure 33b. The same can be realised in Figure 31b for the velocity region of 0.75 between ABV and the ship model.

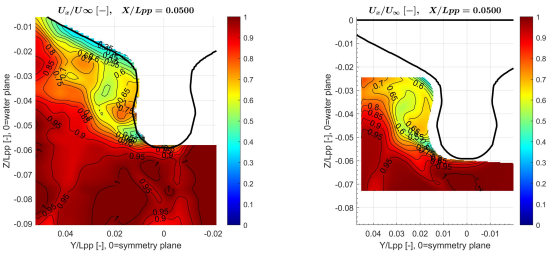

(a) SPIV **(b)** TPIV

Figure 31: U_x at S1 in drift condition

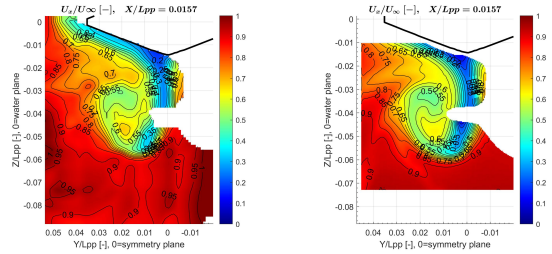

(a) SPIV **(b)** TPIV

Figure 32: U_x at S4 in drift condition

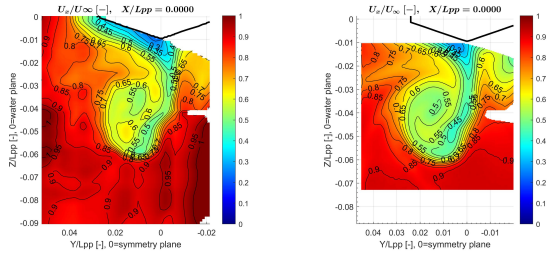

(a) SPIV **(b)** TPIV

Figure 33: U_x at S7 in drift condition

The transverse velocity component U_y is illustrated in Figures 34, 35 and 36 for measurement stations S1, S4 and S7 respectively. The overall velocity profile structure measured by TPIV is similar to the previously measured structure using SPIV. Some discrepancies are realised, such as the low speed component at the ship bottom and at the region vertically below it as well as the high speed component on the port side of the model. Additionally, clear local iso-islands can be detected in the vicinity of the shear layer at measurement stations S4 and S7.

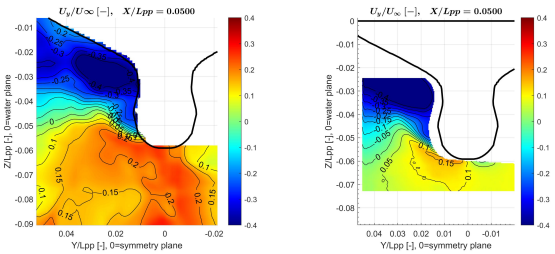

(a) SPIV **(b)** TPIV

Figure 34: U_y at S1 in drift condition

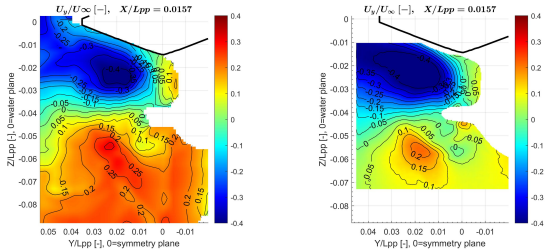

(a) SPIV **(b)** TPIV

Figure 35: U_y at S4 in drift condition

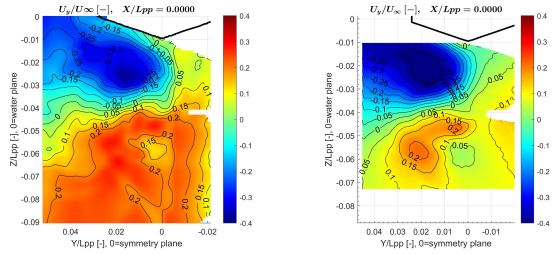

(a) SPIV **(b)** TPIV

Figure 36: U_y at S7 in drift condition

The vertical velocity component U_z is illustrated in Figures 37, 38 and 39 for measurement stations S1, S4 and S7 respectively. No major discrepancies between the TPIV and SPIV results were realised.

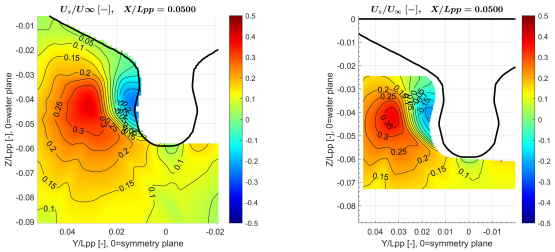

(a) SPIV **(b)** TPIV

Figure 37: U_z at S1 in drift condition

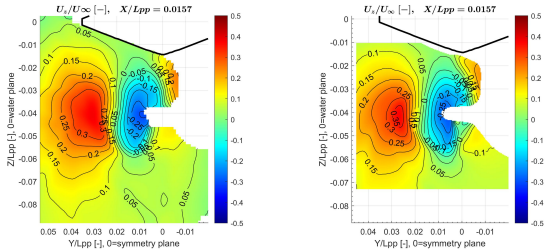

(a) SPIV **(b)** TPIV

Figure 38: U_z at S4 in drift condition

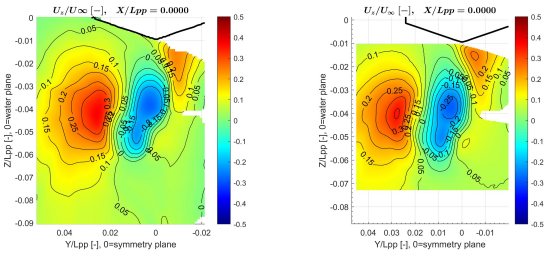

(a) SPIV **(b)** TPIV

Figure 39: U_z at S7 in drift condition

Similar to the straight-ahead case, the vorticity component around the x-axis from TPIV results matches the earlier SPIV measurements qualitatively in regard to position and intensity. Figures 40, 41 and 42 illustrate the comparison for the longitudinal vorticity component between the SPIV and TPIV results in the drift case at the measurement stations S1, S4 and S7 respectively. The results show similar tendencies, as smaller vortical structures in the low-speed region are still realised.

In order to provide more information to understand the vortex structure, the TPIV results for the

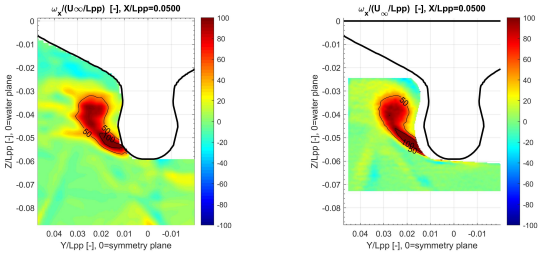

(a) SPIV **(b)** TPIV

Figure 40: ω_x at S1 in drift condition

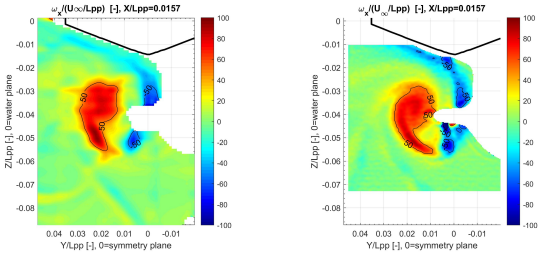

(a) SPIV **(b)** TPIV

Figure 41: ω_x at S4 in drift condition

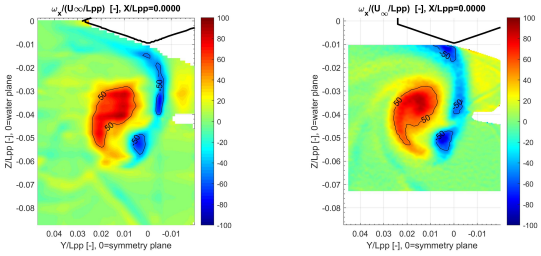

(a) SPIV **(b)** TPIV

Figure 42: ω_x at S7 in drift condition

out-of-plane vorticity components ω_y and ω_z are shown in Figures 43a and 43b for the measurement station S7 respectively. Similar to the straight ahead condition, the vorticity component ω_y is concentrated close to the shear layer and is not directly affected by the drift angle of the model, as the flow field in this region is strongly dominated by the ABV structure. The ω_z vorticity component is still concentrated outside of the ABV core on the port side while it is being seemingly elongated on the starboard side along the whole low-speed region.

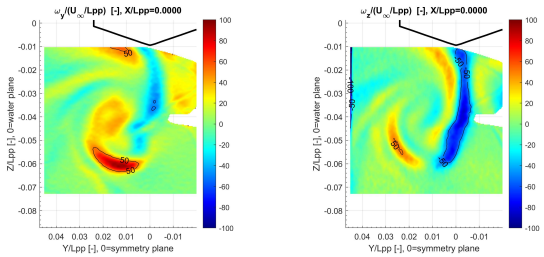

(a) ω_y **(b)** ω_z

Figure 43: ω_y and ω_z at S7 in drift condition

The TKE profiles for the SPIV and the TPIV results in drift condition show multiple interesting features. In the TPIV results for measurement station S1, the TKE contours are extended from the model body and up to the vicinity of the ABV instead of being concentrated in the shear layer in case of the SPIV as shown in Figure 44

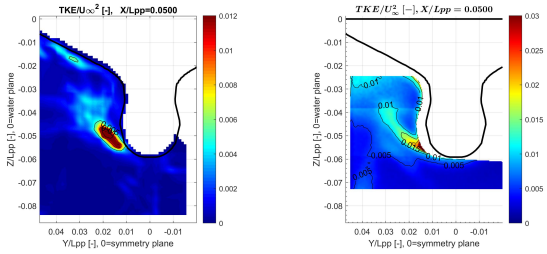

(a) SPIV **(b)** TPIV

Figure 44: TKE at S1 in drift condition

For the measurement stations S4 and S7, as expected, the TKE is high in the model wake region as well as in the shear layer, instead of being concentrated only in the shear layer as previously depicted in the SPIV measurements as shown in Figures 45 and 46 respectively.

Figures 47 and 48 respectively show the diagonal and non-diagonal Reynolds stress tensors at measurement station S7 in the drift condition. The energy content is concentrated in the wake region only in R_{yy}, while it is equally distributed between the wake region and shear layer for R_{xx} and R_{yy}. As expected, the highest

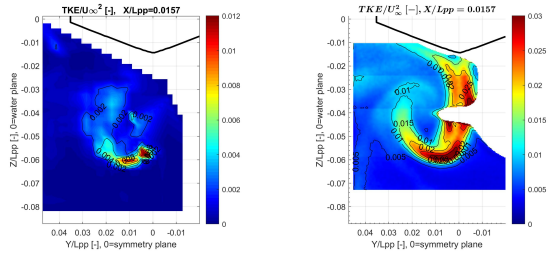

(a) SPIV **(b)** TPIV

Figure 45: TKE at S4 in drift condition

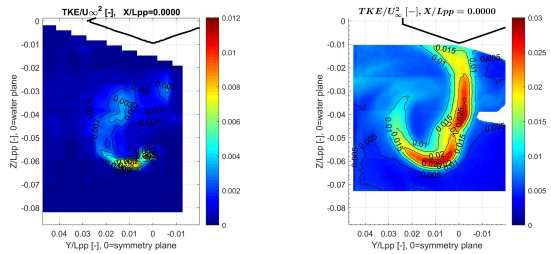

(a) SPIV **(b)** TPIV

Figure 46: TKE at S7 in drift condition

energy content can still be found in the shear layer for R_{xx} compared to the straight ahead condition. However, a second high energy content area can be detected in the wake region for R_{yy}.

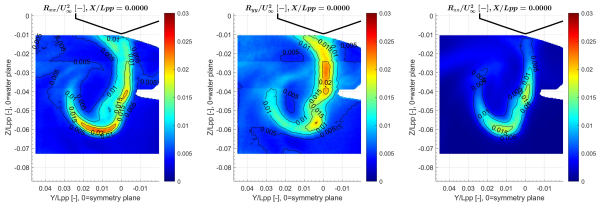

(a) R_{xx} **(b)** R_{yy} **(c)** R_{zz}

Figure 47: Reynolds diagonal tensors at S7 in drift condition

The swirl ($\lambda 2$) for the different measurement stations in the drift condition is shown in Figure 49. The swirling strength is much stronger at measurement station S1 as compared to S7. For the measurement station S4, the maximum swirling strength is located in the outer region of the ABV instead of its geometrical centre.

The helicity for the different measurement stations in the drift condition is shown in Figure 50. The helicity clearly corresponds to the swirling strength shown in Figure 49, in terms that the regions with the maximum swirling strength are also the regions with the maximum helicity. This applies also for measurement station S4, where the maximum helicity is located at the outside side

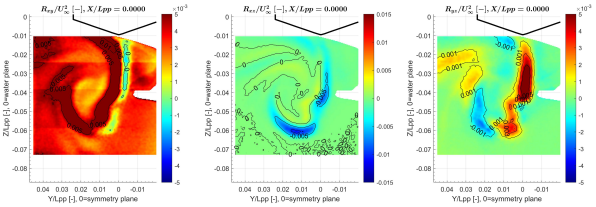

(a) R_{xy} **(b)** R_{xz} **(c)** R_{yz}

Figure 48: Reynolds non-diagonal tensors at S7 in drift condition

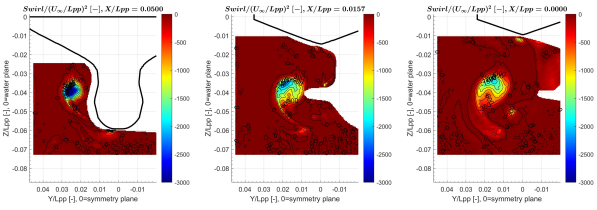

(a) S1 **(b)** S4 **(c)** S7

Figure 49: Swirl ($\lambda 2$) in drift condition

of ABV instead of its geometrical centre.

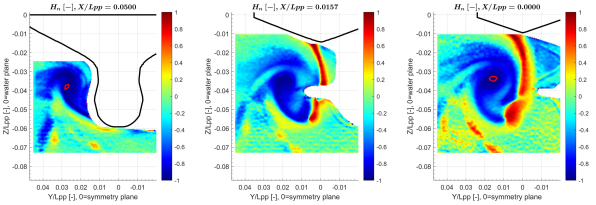

(a) S1 **(b)** S4 **(c)** S7

Figure 50: Helicity in drift condition

Fore-body Side Vortex

In addition to the tracking of the ABV, a second vortex structure (FSV) has been investigated in drift condition. Unfortunately, since there are no available data neither from earlier measurement nor other research institutions, the results are briefly presented without any comparisons. The results for this investigation are acquired through a single measurement window and thus no overlapping techniques were implemented. The formation and detachment of the FSV takes place close to the forward shoulder. Unfortunately, it maintains for a considerable distance close vicinity to the model in the furthest upstream positions, which makes it very challenging to track it experimentally due to the high intensity of laser reflection on the walls of the ship hull. Figure 51 demonstrates the CFD approximation for vorticity magnitude in these upstream positions.

Figure 52 illustrates the axial velocity

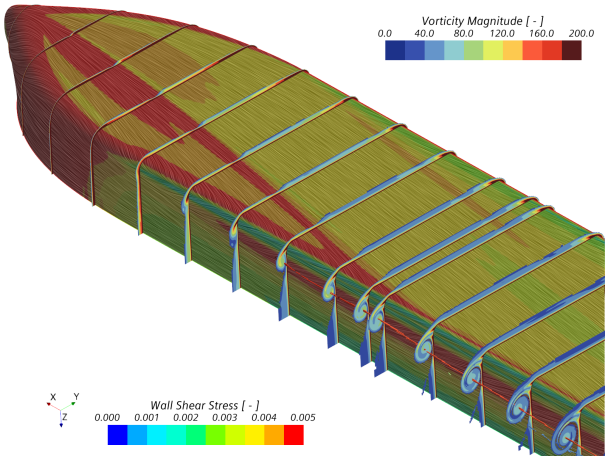

Figure 51: CFD approximation using DDES of FSV separation for vorticity magnitude in drift condition

component for measurement stations S7D, S7, S1 and X0p20. A low-speed region can be easily realised at the vicinity of the FSV. It is also remarkable that the minimum axial velocity component at the FSV core is much higher than the one at the ABV core. It can be seen that the shear layer on the model bottom is directly joined to the FSV, see Figure 52a.

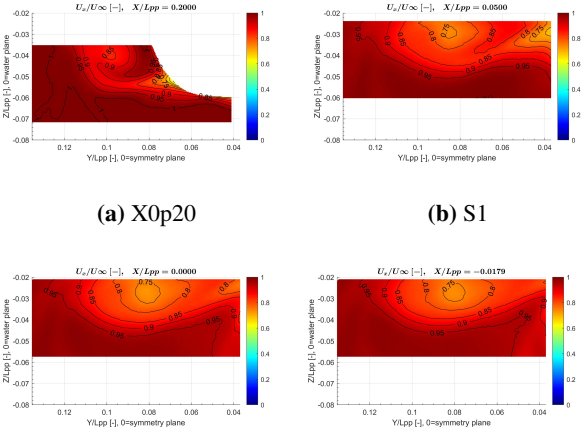

(a) X0p20 **(b)** S1

(c) S7 **(d)** S7D

Figure 52: U_x for FSV in drift condition

Figure 53 illustrates the transverse velocity components for measurement stations S7D, S7, S1 and X0p20. Due to the rotation of the FSV, a seemingly general trend is that the transversal velocity component is directed to starboard side at the upper region of the measurement window, while it is seemingly stationary near the lower region.

Figure 54 illustrates the vertical velocity

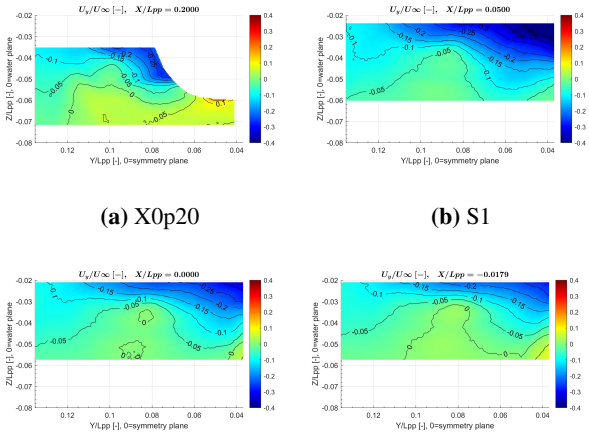

(a) X0p20 **(b)** S1

(c) S7 **(d)** S7D

Figure 53: U_y for FSV in drift condition

components for measurement stations S7D, S7, S1 and X0p20. As the measuring sections are far from the detachment point, the vertical velocity gradient is much weaker in the vicinity of the FSV as compared to the ABV. In Figure 54c, the vertically upwards velocity component presented earlier in the results of ABV is clearly visible at $Y/L_{pp} = 0.04$.

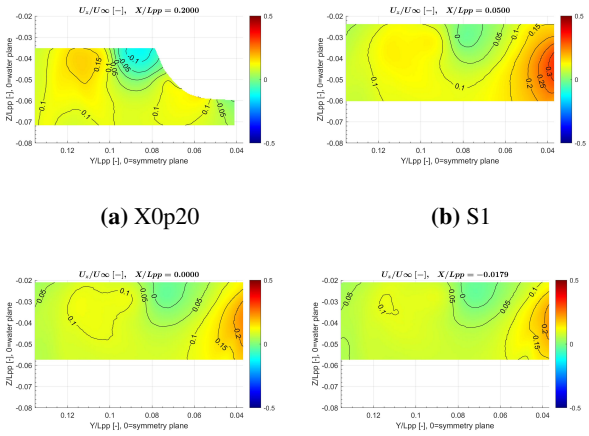

(a) X0p20 **(b)** S1

(c) S7 **(d)** S7D

Figure 54: U_z for FSV in drift condition

The Mean Kinetic Energy (MKE) is computed using equation 2, where (U_x, U_y and U_z) are the velocity components along the streamwise, transverse and vertical directions respectively. It is illustrated in Figure 55.

$$MKE = \frac{1}{2}(U_x^2 + U_y^2 + U_z^2) \tag{2}$$

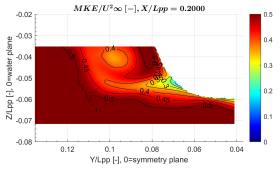

(a) X0p20

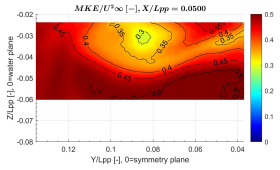

(b) S1

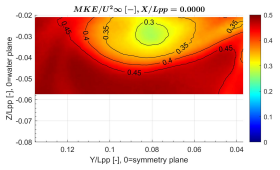

(c) S7

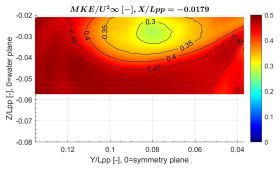

(d) S7D

Figure 55: MKE for FSV in drift condition

As mentioned before, since the FSV separation occurs at the forward shoulder of the ship, its vorticity component ω_x is much weaker at the measuring sections in comparison to the ABV as shown in 56. The Figure 56a shows the interaction between the shear layer on the model bottom and the FSV.

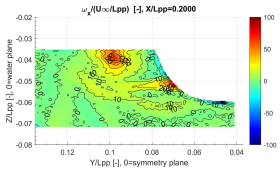

(a) X0p20

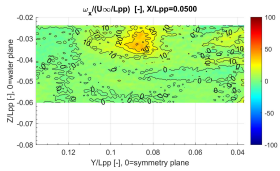

(b) S1

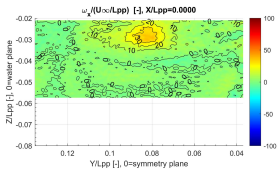

(c) S7

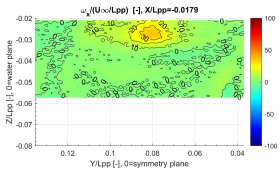

(d) S7D

Figure 56: ω_x for FSV in drift condition

Figure 57 shows the TKE values at the four sections investigated. As shown in Figure 57b, the highest values of TKE can be seen in measurement station S1 as a strong interaction between the shear layer flow, the FSV and the outer flow takes place.

The swirling strength of the FSV is illustrated in Figure 58. The swirl strength drops dramatically as well

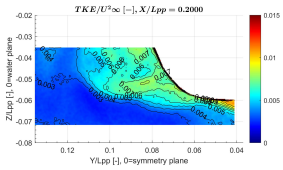

(a) X0p20

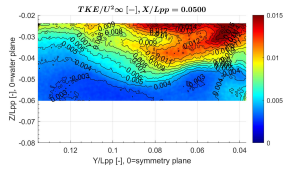

(b) S1

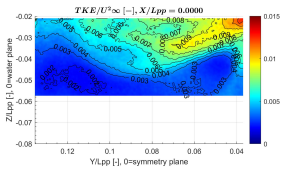

(c) S7

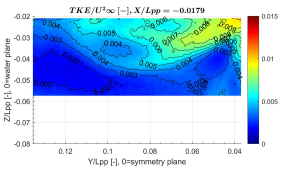

(d) S7D

Figure 57: TKE for FSV in drift condition

from measurement station X0p20 to S7D.

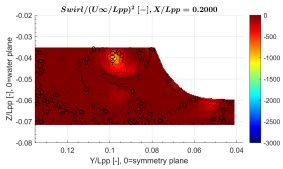

(a) X0p20

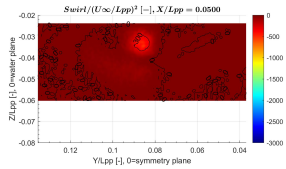

(b) S1

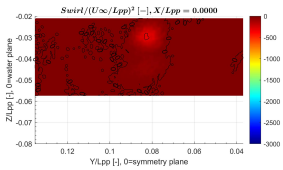

(c) S7

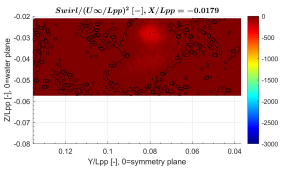

(d) S7D

Figure 58: Swirl for FSV in drift condition

The diagonal and non-diagonal Reynolds stress tensors are illustrated in Figures 59 and 60 respectively.

ABV and FSV vortex interaction

In order to investigate the interaction between ABV and FSV, the same overlapping post-processing process that was used for the individual cases of ABV and FSV is adapted to combine the results of both investigations. The full view of helicity at measurement stations S1, S7 and S7D is shown in Figure 61. The figure illustrates a strong interaction between the two vortices. In the further downstream stations, the interaction between the vortices is much weaker, as expected.

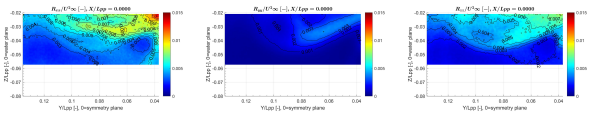

(a) R_{xx} **(b)** R_{yy} **(c)** R_{zz}

Figure 59: Reynolds diagonal tensors for FSV at S7 in drift condition

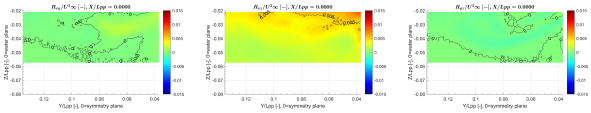

(a) R_{xy} **(b)** R_{xz} **(c)** R_{yz}

Figure 60: Reynolds non-diagonal tensors for FSV at S7 in drift condition

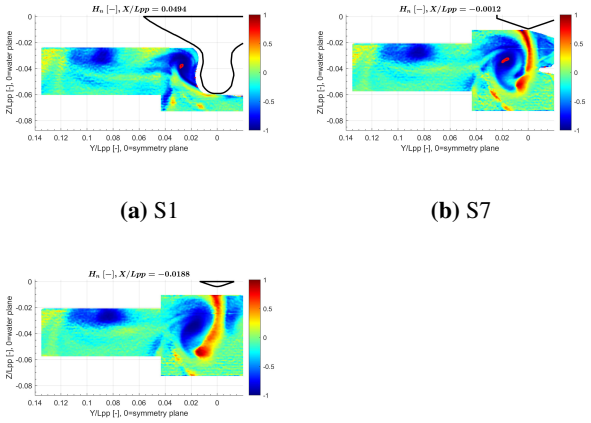

(a) S1 **(b)** S7

(c) S7D

Figure 61: Full view of helicity for ABV and FSV at different measurement stations

The vorticity magnitude at the same measurement stations shows a similar behaviour as shown in Figure 62. A clear interaction within a wide region can be realised with the iso-lines 25 in S1. However, the same iso-line covers a smaller region for the more downstream station S7 and is not discernible in S7D.

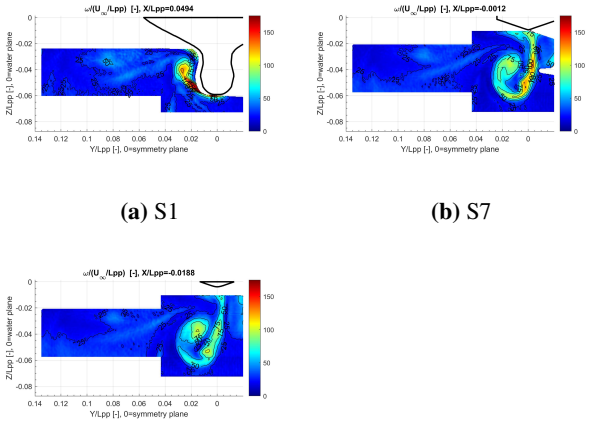

(a) S1 **(b)** S7

(c) S7D

Figure 62: Full view of vorticity for ABV and FSV at different measurement stations

Vortex Tracking

The maximum vorticity around x-axis (ω_x) was used to identify the ABV vortex core and track its position, axial velocity, vorticity and TKE as it progresses downstream in drift condition. Figure 63 illustrates the transverse position of the ABV, which moves closer towards the symmetry plane as it travels further downstream from S1 to S7D. By comparing the TPIV to the SPIV results, despite the initial deviation in the transversal position of around $0.004L_{pp}$ further away from the symmetry plane at measurement station S1, the ABV is located with a deviation of around $0.004L_{pp}$ further closer to the symmetry plane at measurement station S4 and S6. However, the vortex converges to almost exactly the same position measured by SPIV at measurement station S7.

According to the TPIV results, the vertical position of the ABV moves generally upwards as it travels further downstream from S1 to S6 then downwards to S7D as illustrated in Figure 64. The vortex core in the furthest upstream stations S1 to S4D has again a deviation of around 0.004 compared to the previously measured SPIV positions. However, the previous and current results are still within the geometrical vicinity of the vortex maximum vorticity.

The axial velocity component at the points

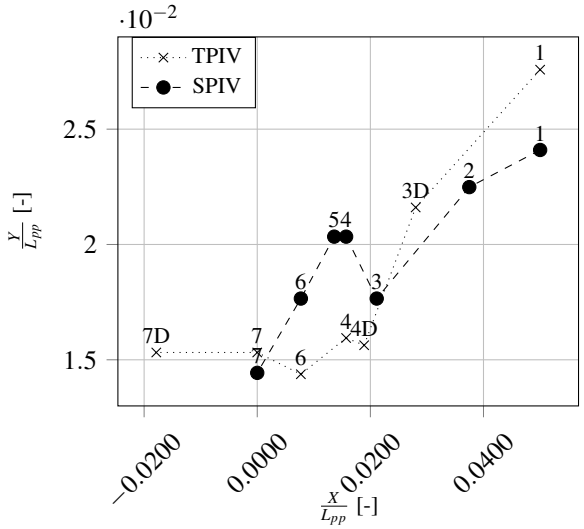

Figure 63: ABV transversal position in drift condition

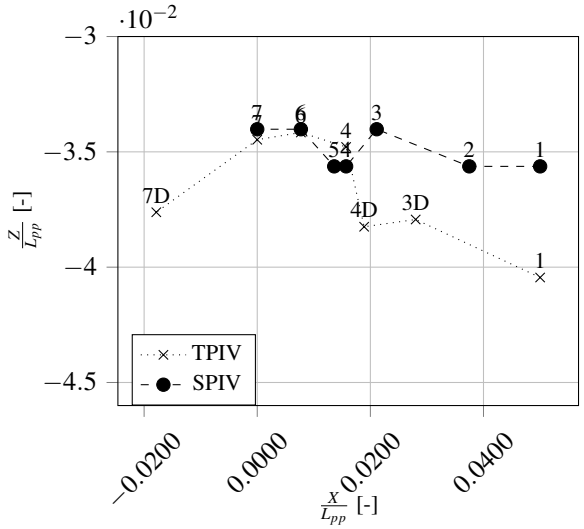

Figure 64: ABV vertical position in drift condition

defined as the vortex core is illustrated in Figure 65. A velocity component of around 3% higher than the SPIV results is noticed at S1. For the rest of the measurement stations, a lower velocity component was realised with a maximum deviation of around 5% at S6.

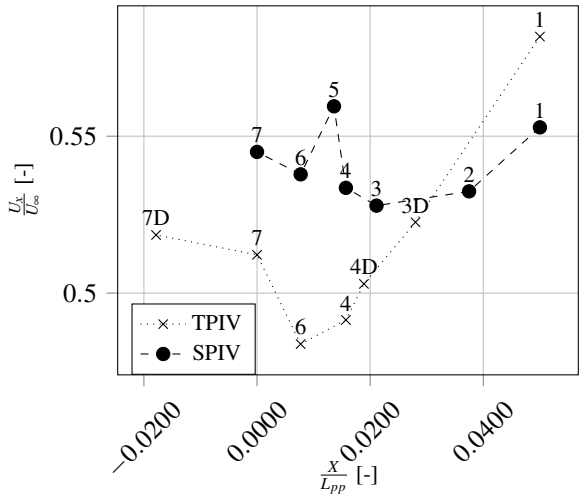

Figure 65: ABV axial velocity component in drift condition

The vorticity component around the x-axis of ABV at the points of maximum helicity is illustrated in Figure 66. The normalised vorticity values for the upstream stations show the same behaviour as the earlier SPIV results, with nearly consistent results at the measurement stations S1 to S4. However, the most downstream stations show a different behaviour, as the vorticity constantly increases from S4 to S7D compared to a decline and then remaining almost constant in the previous measurements.

The TKE of ABV at the points of maximum vorticity component is illustrated in Figure 67. The TPIV results show a general trend of higher TKE compared to SPIV for all measurement stations. The normalised TKE initally increases with around 0.5% from S1 to S3D, then drops to an almost stable value of around 0.7% at the rest of the stations.

SUMMARY AND CONCLUSIONS

In the paper, the results of the experimental investigation conducted using a TPIV system on the wake of a JBC model without appendages are presented for two conditions: straight-ahead and static-drift, in order to provide data with high temporal and spatial resolution which can be used for CFD code validation. Based on this data the vorticity and TKE are evaluated and the position of vortex core in each section is identified.

The results obtained by the TPIV in the case of

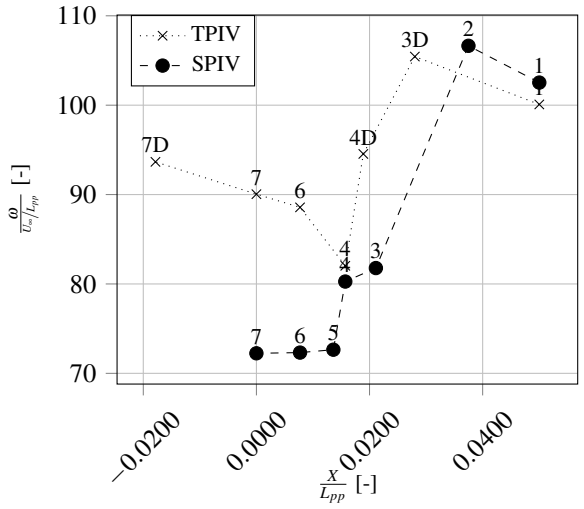

Figure 66: ABV Vorticity component around x-axis in drift condition

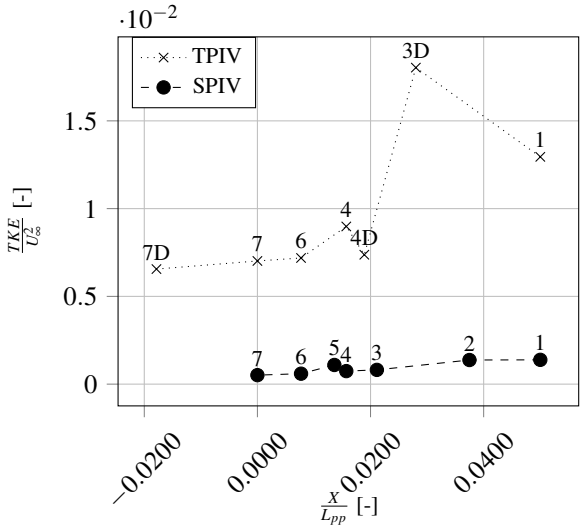

Figure 67: ABV TKE in drift condition

straight ahead condition are presented for the different sections. The measured values at stations S4 and S7 were compared to the earlier results obtained with SPIV in the same facility and to the results of the experimental investigation conducted by NMRI and OU in a towing tank. Minor deviations from the previous SPIV results for the longitudinal and transversal velocity components as well as the vorticity component around the x-axis were realised. TKE level measured by TPIV is higher than that obtained by SPIV. However, the TPIV results agree with the results presented by NMRI and OU considering the vorticity around the x-axis and the higher energy content in TKE. Since the investigations conducted by NMRI and OU were in a towing tank, different test conditions and approaches were adopted compared to the current investigation. Acquiring the results with matching patterns and very similar TKE level would give the TPIV results higher credibility compared to the previous SPIV ones.

In the static drift condition, 7 and 6 measurement stations were investigated for ABV and FSV respectively. By comparing qualitatively the results for ABV using TPIV to the earlier SPIV results, good agreement regarding the local flow fields was found. The TPIV provides more clear energy profiles regarding TKE results. Data from other research institutions is required for comparison of FSV results. The interaction between both vortices ABV and FSV is briefly explored. Strong interaction between both vortical structures was found in the furthest upstream positions. As both vortices travel further downstream, the interaction is not discernible any more. Further investigation is required regarding the interaction between FSV and ABV as well as the influence of the interaction on the shift of the lateral positions of the vortex core. The results for vortex tracking in the drift condition is provided as a comparison between the TPIV and SPIV results.

Since the spatial resolution is a clear disadvantage of TPIV against SPIV systems using the same hardware, an approach is adopted in which interrogation areas with higher overlap were used to compensate for such decrease in the spatial resolution. This approach would entail longer evaluation time, but it is proven successful to reach a sufficiently comparable spatial resolution. The approach is limited by the particle size of the seeding, the focal length of the used lenses and the separation time between frames. However, all these factors can be optimized during the measurement phase. The higher temporal resolution of the TPIV system ($500Hz$) allowed an efficient acquisition of the vorticity and TKE fields, which were hardly obtained with much slower SPIV system ($7.25Hz$). The temporal resolution is limited by the available storage capacity since a higher temporal resolution requires enormous capacity

to capture sufficient data in order to reach statistical convergence. Such trade-off has to be optimized for each individual measurement.

Finally, a second approach which was adopted is the measurement of neighbouring overlapping windows then post-processing them to achieve a total larger captured volume. The overlapping process proved efficient regarding the averaged flow fields. Some discrepancies in the turbulent data were realized in the overlapped regions which can be attributed to the lower uncertainty at the edge of the individual measurement windows and to the different time-frames of conducting the sequential individual measurements.

ACKNOWLEDGEMENTS

The authors are grateful to the German Federal Ministry for Economic Affairs and Climate Action for the fund provided for the project *PSDMan* as a part of the program "Maritime Forschungsstrategie 2025". For their excellent cooperation in the project, the authors would like to also thank the industrial partners: Becker Marine Systems GmbH (www.becker-marine-systems.com), IBMV Maritime Innovationsgesellschaft mbH (www.ibmv.de) and Schiffbau Versuchsanstalt Potsdam GmbH (www.sva-potsdam.de).

REFERENCES

26th ITTC, "Recommended Procedures and Guidelines, Ship models", International Towing Tank Conference, 2011 (URL January 2022: http://ittc.info).

27th ITTC, "Recommended Procedures and Guidelines, Guideline on the Uncertainty Analysis for Particle Image Velocimetry", International Towing Tank Conference, 2014 (URL January 2022: http://ittc.info).

Abdel-Maksoud, M., Müller, V., Xing, T., Toxopeus, S., Stern, F., Petterson, K., Tormalm, M., Kim, S., Aram, S., Gietz, U., Schiller, P. and Rung, T., "Experimental and Numerical Investigations on Flow Characteristics of the KVLCC2 at 30° Drift Angle", SNAME Maritime Convention, SMC 2015, 2016, pp. 139-164

ASME Test Code, " Test Uncertainty, Performance Test Codes, PTC 19.1-1998", The American Society of Mechanical Engineers, 1998.

ASME Test Code, " Test Uncertainty, Performance Test Codes, PTC 19.1-2005", The American Society of Mechanical Engineers, 2006.

Bhushan, S., Yoon, H., and Stern, F., "Detached eddy simulations and tomographic PIV measurements of flows over surface combatant 5415 at straight-ahead and static drift conditions". Ocean Engineering, Vol. 238, pp. 109658, 2021

Broglia, R., Aloisio, G., Falchi, M., Grizzi, S., Zaghi, S., Felli, M., ... and Stern, F., "Measurements of the velocity field around the DELFT 372 catamaran in steady drift" Proceedings of the 29th symposium on naval hydrodynamics, Gothenburg, 2012.

Egeberg, T. F., Yoon, H., Stern, F., Pettersen, B., and Bhushan, S., "Vortex shedding from a ship hull by means of tomographic PIV", International Conference on Offshore Mechanics and Arctic Engineering, Vol. 45509, American Society of Mechanical Engineers, 2014.

Feder, D. F., Shevchuk, I., Sahab, A., Gerwers, L., and Abdel-Maksoud, M., "Fore-Body Side Vortex of KVLCC2 at 30° Drift: A Trailing Vortex Resolved with DES and Compared to PIV Data", Open Journal of Fluid Dynamics 9.4, 2019, pp. 303-325.

Hino, T., Hirata, N., Ohashi, K., Toda, Y., Zhu, T., Makino, K., Takai, M., Nishigaki, M., Kimura, K., Anda, M., and Shingo, S., "Hull form design and flow measurements of a bulk carrier with an energy-saving device for CFD validations", Proc. 13th International Symposium on Practical Design of Ships and Other Floating Structures (PRADS'2016), Copenhagen, Denmark, 2016.

Hino, T., Stern, F., Larsson, L., Visonneau, M., Hirata, N., and Kim, J., Numerical Ship Hydrodynamics: An Assessment of the Tokyo 2015 Workshop, Vol. 94, Springer Nature, 2017.

Jeong, J., and Hussain, F., "On the identification of a vortex". Journal of fluid mechanics, Vol. 285, pp. 69-94, 1995.

Jufuku, N., Hori, M., Itou, S., Toda, Y., and Hinatsu, M., "SPIV stern flow measurement around operating propeller for with and without duct condition of Japan bulk carrier". Conference Proceedings of the Japan Society of Naval Architects and Ocean Engineers, Vol. 21, 2015, pp. 309-312.

Levy, Y., Degani, D., and Seginer, A. "Graphical visualization of vortical flows by means of helicity". AIAA journal, Volume 28, No. 8, pp. 1347-1352, 1990.

Merlet, J.P., "Kinematics of the wire-driven parallel robot MARIONET using linear actuators", 2008 IEEE International Conference on Robotics and Automation, 2008, pp. 3857-3862

Shevchuk, I., Sahab, A., Stern, F., and Abdel-Maksoud, M., ”Experimental and numerical studies of the flow around the JBC hull form at straight ahead condition and 8 drift angle”, Proc. the 33rd Symposium on Naval Hydrodynamics Osaka, Japan, 2020.

Sumislawski, P., Sahab, A., Shevchuk, I., and Abdel-Maksoud, M., ”Numerical investigation of the JBC hull and propeller interaction at static drift condition”, Proc. the 34th Symposium on Naval Hydrodynamics Washington DC, USA, 2022 (Submitted).

DISCUSSION 1

Discusser: Rickard Bensow
Discusser information: Dept. Mechanics and Maritime Sciences, Chalmers University of Technology, Göteborg, Sweden

The results presented in this paper will certainly be valuable to the community, increasing the understanding of the structure of the vortex system and provide detailed flow information for CFD validation.

Not being an expert in experimental techniques, I'm however worried about the sometimes rather large differences between the older SPIV and the newer TPIV results. The discrepancies seem larger than the reported uncertainty and not fully explained by the differences mentioned in experimental set-up. Could you please comment on how we from the CFD community should interpret these differences?

I'm curious to know if you did (or are planning) any flow visualisations, smoke or other techniques? It would be interesting to get an impression of the instantaneous flow field in the two conditions. This could perhaps also be extended to the formation of the FSV.

AUTHOR'S REPLY 1

Thank you for your valuable comments and questions. Regarding the discrepancies between the results obtained with the older SPIV and newer TPIV results, the two investigations were conducted on different JBC models. Since both models are covered by a Rhodamine layer to reduce the impact of the reflected laser on the hull of the models and due to the complexity of implementing the Rhodamine layer, the surface roughness of both models are not identical. Unfortunately, due to limited availability at the testing facility to measure and quantify the surface roughness, it is not considered in the uncertainty analysis in both investigations. Another important factor that caused such discrepancy in the second order quantities is the number of overlapped measurement windows. The prior SPIV results were synthesized from 15 measurement windows in comparison to only 3 measurement windows in case of the TPIV results. These measurement windows were captured in consecutive manner and not at the same instant and therefore the dynamic features of the flow might have changed between one measurement window and the neighbouring ones. That higher count of overlapped measurement windows along with the slower measurement rate lead to high difficulty in tracking dynamic changes in the flow and hence the distorted results for the driven quantity of the turbulence kinetic energy in case of SPIV.

Regarding flow visualizations, no flow visualizations were planned within the work packages of the current investigation since the measurement positions were well defined in advance from the prior measurements. However, flow visualizations were conducted on another very similar model named "Dummy JBC model". The dummy model has the same overall hull structure of the regular JBC but the middle straight part is cropped. The flow structures for the dummy and regular JBC are not identical but the overall features are comparable to each other. While the investigated JBC model is a double hull model mirrored at the water level, the dummy model is only single hull model and therefore was fixed on the floor of the testing section. Figure 68 shows the flow visualization at the measurement station S7 for the dummy model in the straight ahead condition. This figure is comparable to figures 22 and 24 as the flow structure representing the shear layer is clearly visible at this position. More flow visualization results are available for the dummy model at various measurement stations and with different combinations of appendages (Rudder, Propeller and Duct).

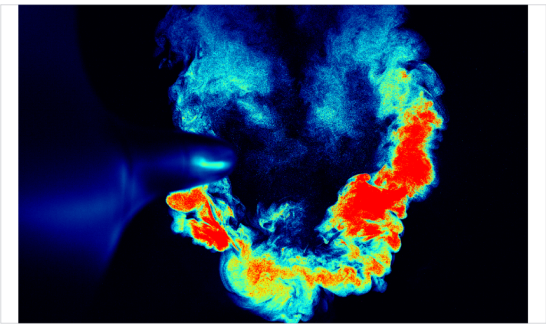

Figure 68: Flow visualization at S7 for dummy JBC model in straight ahead condition

DISCUSSION 2

Discusser: Michel Visonneau
Discusser information: CNRS, High Reynolds Incompressible Flows and Coupling LHEEA Lab, Nantes, France

This very interesting paper shows a new experimental campaign conducted by TUHH on the JBC with the help of a powerful new TPIV system. The velocity and turbulence fields are investigated in the wake of the JBC without appendages at straight ahead and static drift conditions. Some new and very valuable informations are provided, concerning the structure of the main vortices influencing the wake. These new measurements provide a very useful addition to the previous experimental campaigns conducted by NMRI and Osaka University for the Tokyo 2015 Workshop on Numerical Ship Hydrodynamics and can be used for the next edition of this workshop. During the discussion of the T2015 CFD contributions, many participants

reported problems of non-linear convergence of RANSE computations which were attributed to a likely large scale unsteady behaviour of the wake, probably related with the high C_B coefficient characterizing this hull. Have you confirmed this feature? Is the ABV vortex perfectly steady or does it periodically move when a time averaging of experiments is performed with various time scales? Another hot topic is the tke distribution in the ABV vortex. It seems that your TPIV measurements confirm the existence of a region of high tke being concentrated only in the shear layer as indicated in Fig.44. However, the tke values observed in the core of the ABV vortex (being identified as the point where ω_x is maximum) in these TPIV experiments are probably between 0.015 and 0.020, which is higher than what was computed by RANS turbulence models but smaller than what was provided by LES or hybrid RANS/LES turbulence closures during the T2015 workshop. These new TPIV measurements might clarify a controversy which emerged during the discussion of the T2015 results. Can you comment about that and explain how these results enrich the analysis carried out during the assessment of the Tokyo 2015 workshop? Since you have access to the six components of the Reynolds stress tensor, I would also recommend to draw the local Lumley triangles for each experimental section to characterize more precisely the evolution of the turbulence anisotropy during the progression of this vortex.

AUTHOR'S REPLY 2

Thank you for your valuable comments and questions.

The instantaneous fields obtained at S7' in the straight ahead condition were further investigated to identify if a wandering behaviour exists. Figure 69 shows the vortex core position for the ABV vortex on the port side of the model at S7' in straight ahead condition for 6 consecutive recordings. The vortex core was defined as the point with the maximum vorticity around x-axis (ω_x). The iso-lines represents the averaged vorticity around x-axis (ω_x) for the complete dataset at this measurement station. The red circle represents the vortex core position in the 21st recording while blue circles show the vortex core position in the prior 5 recordings.

Figures 70 and 71 illustrate the Fast Fourier Transformation (FFT) for the y- and z-position of the vortex core respectively. No clear main frequency or frequency range were identified. Similarly in figure 72 to 74, the results of the FFT anaylsis of the velocity components show no dominant main frequency or frequency range. However, a slightly higher amplitude can be noticed at $f = 21Hz$ in figures 70, 71 and 74. The ABV vortex can be then safely considered as highly unsteady. For a proper comparison with

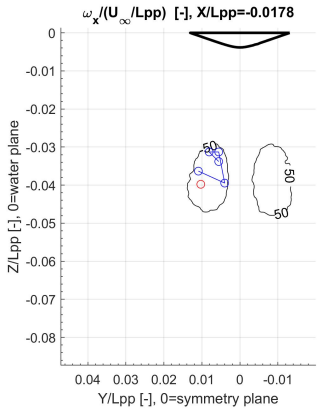

Figure 69: Vortex core position for ABV at S7' in straight ahead condition for the recordings 16 to 21

the CFD investigations, it is advisable to perform a wandering correction for both the experimental data and the computed CFD results.

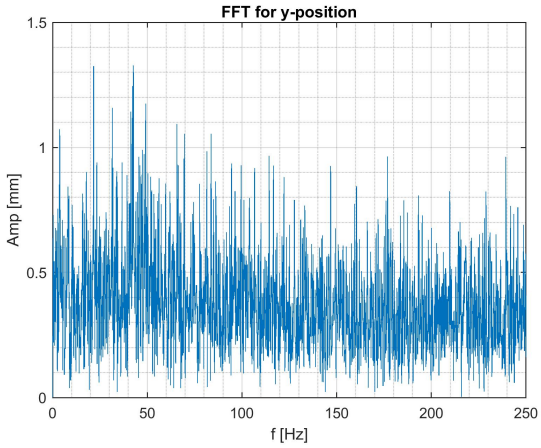

Figure 70: FFT for y-position

Figure 75 shows the turbulence triangle for the measured points along the horizontal line $\frac{Z}{L_{pp}} = -0.0407$ at the measurement station S7 in the straight ahead condition. The figure can be divided into 3 main regions; the free-stream $\frac{Y}{L_{pp}} = [0.025, 0.045]$, the ABV $\frac{Y}{L_{pp}} = [0.005, 0.01]$ and the wake $\frac{Y}{L_{pp}} = [-0.003, 0.003]$ as depicted in figure 76.

The free-stream region is illustrated in figure 77. The figure shows the measured points located in the axisymmetric expansion region and seemingly close to the one-component boundary. Despite the turbulence values are very low in that region, the turbulence in stream-wise direction is relatively higher than the other two directions and as the points are getting closer to the ABV region, the turbulence in the transverse direction gets stronger so that

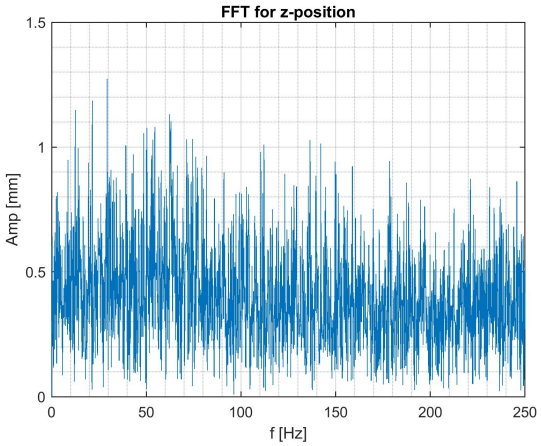

Figure 71: FFT for z-position

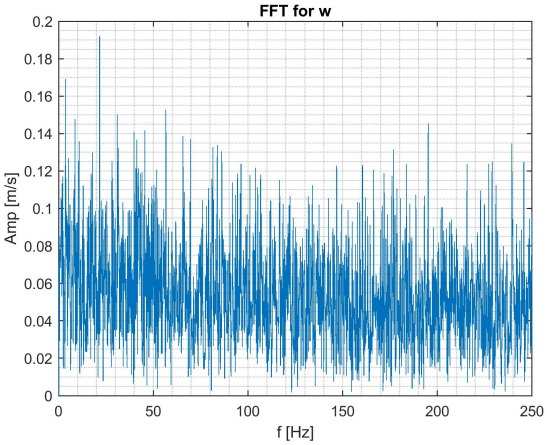

Figure 74: FFT for vertical velocity component

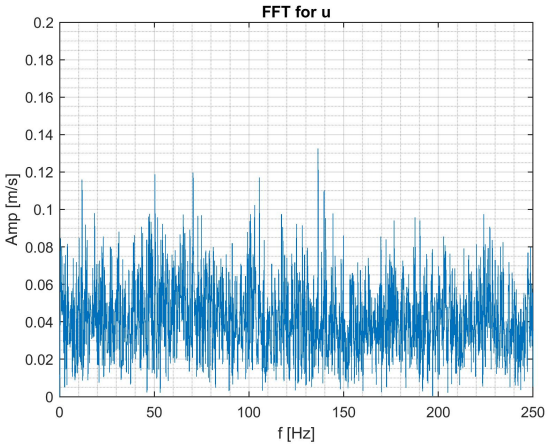

Figure 72: FFT for longitudinal velocity component

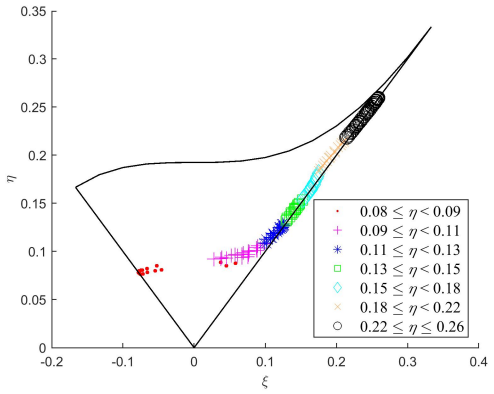

Figure 75: Turbulence triangle along the line $\frac{Z}{L_{pp}} = -0.0407$ at S7 in straight ahead condition

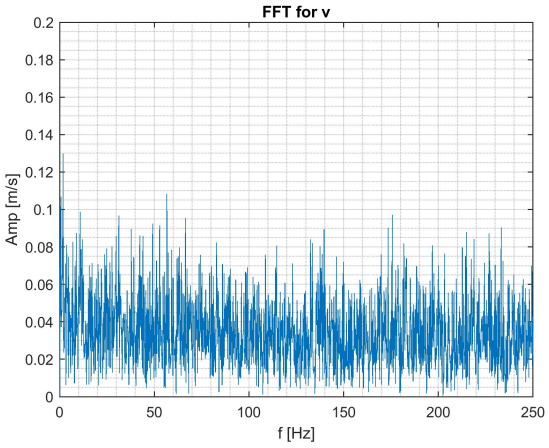

Figure 73: FFT for transversal velocity component

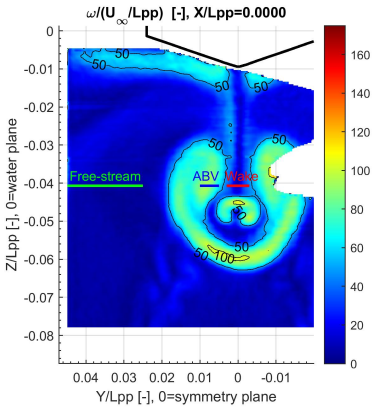

Figure 76: The 3 main regions: the free-stream $\frac{Y}{L_{pp}} = [0.025, 0.045]$, the ABV $\frac{Y}{L_{pp}} = [0.005, 0.01]$ and the wake $\frac{Y}{L_{pp}} = [-0.003, 0.003]$

it starts to impose the expansion behaviour.

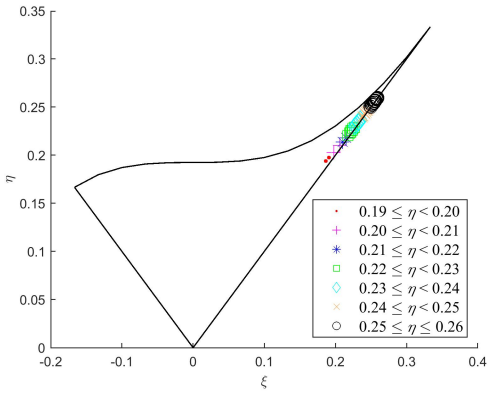

Figure 77: Turbulence triangle along the line $\frac{Z}{L_{pp}} = -0.0407$ at S7 in straight ahead condition in the free-stream region, $\frac{Y}{L_{pp}} = [0.025, 0.045]$

The ABV region is illustrated in figure 78. The figure shows the measured points located in the axisymmetric contraction region in which the turbulence in the stream-wise and transverse directions have the major impact.

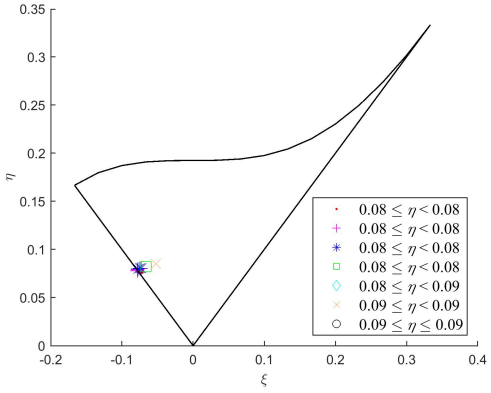

Figure 78: Turbulence triangle along the line $\frac{Z}{L_{pp}} = -0.0407$ at S7 in straight ahead condition in the ABV region, $\frac{Y}{L_{pp}} = [0.005, 0.01]$

The wake region is illustrated in figure 79. The figure shows the measured points located in between the plain-strain and the axisymmetric expansion region. This region is between the two ABVs on port side and starboard side of the hull and therefore it is in a transient state in which the turbulence is axisymmetric expansion before moving to the axisymmetric contraction in the opposite ABV region again.

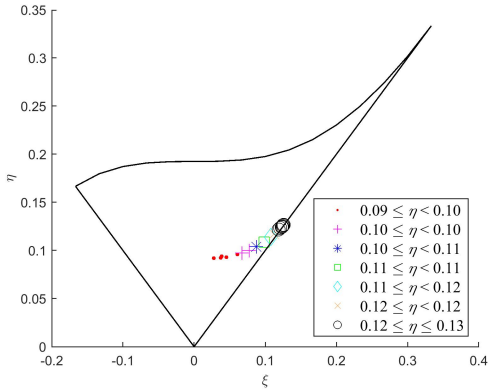

Figure 79: Turbulence triangle along the line $\frac{Z}{L_{pp}} = -0.0407$ at S7 in straight ahead condition in the wake region, $\frac{Y}{L_{pp}} = [-0.003, 0.003]$